Memory-augmented cognitive radar for obstacle avoidance using nearest steering vector search

Guo, Liyong; Antoniou, Michail; Baker, Chris

DOI:
10.1049/rsn2.12012

Document Version
Publisher's PDF, also known as Version of record

Citation for published version (Harvard):
Guo, L, Antoniou, M & Baker, C 2021, 'Memory-augmented cognitive radar for obstacle avoidance using nearest steering vector search', *IET Radar, Sonar and Navigation*, vol. 15, no. 1, pp. 51-61.
https://doi.org/10.1049/rsn2.12012

Received: 3 September 2020 | Revised: 4 October 2020 | Accepted: 4 November 2020

DOI: 10.1049/rsn2.12012

ORIGINAL RESEARCH PAPER

The Institution of Engineering and Technology WILEY

Memory-augmented cognitive radar for obstacle avoidance using nearest steering vector search

Liyong Guo[1] | Michail Antoniou[2] | Christopher J. Baker[2]

[1]Key Laboratory of Electronic and Information Technology in Satellite Navigation, Beijing Institute of Technology, Ministry of Education, Beijing, China

[2]Department of Electronic, Electrical and Systems Engineering, School of Engineering, University of Birmingham, Birmingham, UK

Correspondence

Michail Antoniou, Department of Electronic, Electrical and Systems Engineering, School of Engineering, University of Birmingham, Birmingham, UK.
Email: M.Antoniou@bham.ac.uk

Funding information

China Scholarship Council; National Key R&D Program of China, Grant/Award Number: Grant No. 2018YFE0202101, 2018YFE0202102

Abstract

This study describes a cognitive radar architecture with application to real-time obstacle avoidance in mobile robotic platforms. The concept of a world memory map is introduced as a means of providing an enhanced perception of the environment around the robotic platform. This is combined with a specially designed obstacle avoidance algorithm, Nearest Steering Vector Searching, all capable of operating in real-time. The study analytically derives the radar signal processing algorithm, starting from range-angle maps, so that a collision free course to a set destination point can be robustly navigated. Finally, the performance of this cognitive approach is examined through a number of proof-of-concept experiments using a commercial off-the-shelf radar mounted on a mobile ground robotic platform.

1 | INTRODUCTION

Obstacle avoidance, when navigating unknown environments, is a fundamental problem in mobile robotics and has been the subject of extensive recent research [1]. To achieve collision-free movement, a mobile platform relies on onboard sensors to perceive its surroundings, detect obstacles in its path, and inform appropriate evasive action and path planning [2]. Different types of sensors have been considered for this purpose, such as optical, ultrasonic, and lidar. Each of these operates on different physical principles and therefore have different relative merits and drawbacks.

Radar systems are another type of sensor that can also be used for this purpose. Compact radar arrays can be incorporated into a mobile platform to generate range-angle backscattered information enabling the detection of objects. However, despite considerable research [3–6], radar systems have experienced substantially less uptake for autonomous mobile robotics. This is partly because the information generated by radar systems generally has lower resolution and accuracy than other sensing modalities. It is also partly because the complexity of radar scattering makes reliable information extraction more challenging. However, radar has the advantage of working regardless of day or night times and in all weathers. Hence, for many applications radar is the only viable sensor.

In this study cognitive radar [7] architectures are considered as a potential solution able to better overcome the challenges mentioned above. To address radar scattering uncertainties, caused by characteristics such as low target reflectivity and radar cross-section fluctuations, certainty grids are introduced. The certainty grids are also used to cope with the fact that obstacles may stray outside the radar field of view as the robot navigates and changes orientation. In addition to making detection decisions, the radar can also dynamically increase confidence of an obstacle's presence by creating and exploiting a form of 'short-term' or 'active' memory. This has some similarities to environmental dynamic database concepts used as primary components of knowledge-aid methods (e.g. [8]). This overall concept was tested in recent similar work [9]. It was experimentally shown that having a memory-aided architecture substantially reduces the number of collisions compared to not employing memory at all. However, collisions happened in some of the trials and the trajectories of the robot were not smooth. Here in this study, short-term memories are generated from prior radar data and formed into 'world memory map' (WMM) [10]. The process is part inspired by the in-motion mapping concept [11]. However, the WMM technique accumulates

measurements over a period during the motion of the robot and then uses the cumulative information to increase confidence as to the presence or absence of an object. This is used as a core component of our cognitive radar architecture where we seek to create a memory-aided radar mapping to improve the instantaneous perception. This is therefore quite different to other research that has attempted to exploit full transmit-receive adaptation for applications such as tracking [12–14] or biomimetic steering using echoic flow [15].

Using such a cognitive radar approach to enhance the perception of the robot's surroundings, robust and reliable obstacle avoidance techniques can then be implemented. To decrease the computational load, a smaller active WMM region in front of the sensor is used to detect obstacles, rather than the whole field of view [16]. To determine suitable collision-free routes, a diagram-based obstacle avoidance method is employed. This has the additional benefit that the radar is able to set appropriate safety distance limits from obstacles thus diminishing the chances of a collision. This is unlike conventional techniques such as the nearness diagram [17] or follow-the- gap [18] methods. To achieve collision-free navigation, a suitable means of converting the WMM into an avoidance route is also needed.

This study develops and examines a memory-aided cognitive radar architecture to produce reliable maps (perceptions) of its surroundings. This enhanced perception is then used to develop a simple strategy for obstacle avoidance. The radar signal processing to facilitate both functions is described. Subsequently, the performance of the proposed cognitive system, comprising the robotic platform and the radar, is investigated experimentally. The radar is an off-the-shelf, co-located multiple-input-multiple-output (MIMO) radar and this is integrated onto a mobile robotic platform that has the goal of moving from a starting position to a chosen destination in the presence of fixed obstacles. There is a taxonomy framework to classify cognitive radar systems [19]. The levels of cognition for the radar system in this study are considered as (planning:memory:decision) = (4:4:3). The levels represent the classification of cognitive elements within Intelligent Radar systems. The higher the level, the higher the degree of intelligence. The levels of the proposed radar system are not fixed. For example, by applying path-planning algorithm based on WMM, the planning level will increase accordingly.

The study is organized as follows: Section 2 introduces the cognitive radar signal processing method. The proposed real-time obstacle avoidance method is developed in Section 3. The experimental campaign and its results are shown in Section 4 and the conclusions are in Section 5.

2 | COGNITIVE RADAR SIGNAL PROCESSING FOR RADAR PERCEPTION

2.1 | Brief description of the robot working process

A simplified flowchart of how the robot works with the WMM is depicted in Figure 1 and comprises the following steps:

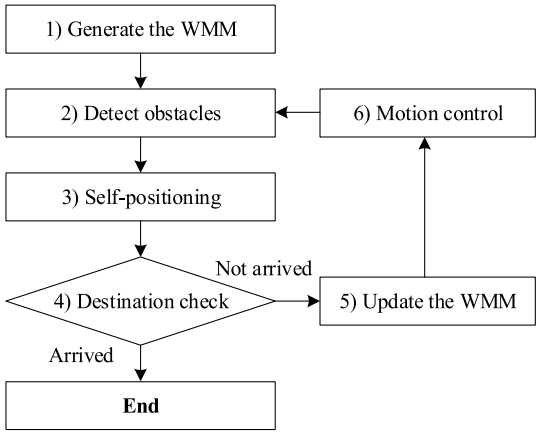

FIGURE 1 Flowchart to show how the robot works with the world memory map (WMM)

1) Create an initial 'memory map' of the entire area surrounding the robot. The resolution of the memory map is determined by the range and angle resolution of the radar
2) Radar determines the positions of any detected obstacles according to the radar data
3) Determine the current absolute position of the robot
4) Check if the robot has arrived at the final destination. If the robot has arrived at the final destination, stop. Otherwise, update the WMM according to the detected obstacles
5) Based on the information of obstacles from the WMM, determine the direction for the robot to move and start to move in that direction
6) Repeat step 2) and continue to repeat the cycle until the robot reaches its final destination

In all of the above it is assumed that all obstacles are static and only the robot is in motion.

2.2 | Range-angle mapping

This section describes the formation of a range-angle radar map from a single radar pulse, from a single robot position. This is the fundamental data block from which information is derived enabling the location of obstacles in view of the radar sensor. The radar used is a MIMO array, and although the theory of object location from a MIMO array is well-known [20], it is included here for completeness. Note, conventional single beam radars or phased array radars could also be used.

The transmitted signal is a linear frequency modulated continuous waveform (LFMCW). The echo signals from a point target, at each receiver and after stretch processing and quadrature demodulation can be written as (ignoring constant amplitude and phase terms):

$$s_B[n] = \exp\left(j2\pi f[n]\left[\frac{2r}{c}\right]\right), n = 0, 1, 2, \ldots, N-1, \quad (1)$$

where $f[n] = f_0 + \frac{\beta n}{N} = \frac{c}{\lambda[n]}$ is the time-varying frequency of the receive signal, β is the effective sweep bandwidth, N is the number of recorded samples, r is the target range and c is the speed of light.

Consider a co-located MIMO array with N_T Transmitters (Tx) and M_R receivers (Rx) as shown in Figure 2. The Rx elements form a filled sub-array whose elements are separated by a distance, d_R, and the Tx elements are separated by a distance, d_T. The total received echo can be written as:

$$s_{MIMO}[n, m_T, m_R] = \exp\left(j2\pi f[n]\frac{d_T[m_T]}{c}\sin(\alpha)\right) \cdot \exp\left(j2\pi f[n]\frac{d_R[m_R]}{c}\sin(\alpha)\right)s_B[n], \quad (2)$$

where $m_T = 0, 1, \ldots, N_T - 1$, $m_R = 0, 1, ..., M_R - 1$ and α is the target angle.

This allows creation of a virtual filled array of $(N_T \times M_R)$ elements with a separation of d_R. The MIMO steering vector is

$$\boldsymbol{a}_{MIMO}(n, \alpha) = \left[e^{j2\pi\frac{d_{VA}[0]}{\lambda[n]}\sin\alpha}\, e^{j2\pi\frac{d_{VA}[1]}{\lambda[n]}\sin\alpha} \mathrm{K} e^{j2\pi\frac{d_{VA}[M_{VA}-1]}{\lambda[n]}\sin\alpha}\right]^T, \quad (3)$$

where $d_{VA} = d_R$ is the virtual array antenna distance to the reference antenna, $M_{VA} = N_T \times M_R$ is the total number of the virtual array elements and $[\cdot]^T$ means the transpose operation.

The receive signal snapshot vector is

$$\boldsymbol{x}[n] = \boldsymbol{a}_{MIMO}(n, \alpha_0)s_B[n], \quad (4)$$

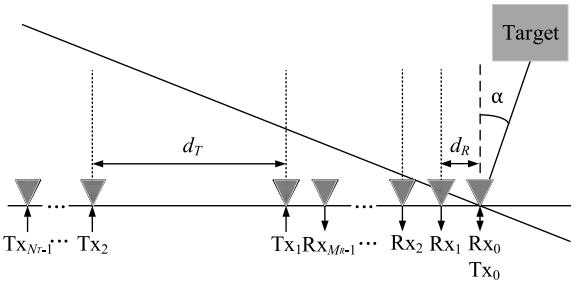

FIGURE 2 MIMO array configuration. It is a co-located MIMO array with N_T Transmitters (Tx) and M_R receivers (Rx); MIMO, multiple-input-multiple-output

where $\boldsymbol{x}[n]$ is a $M_{VA} \times 1$ vector and α_0 is the target azimuth.

The estimate of the signal coming from an angle α is

$$\hat{s}_\alpha[n] = \frac{1}{M_{VA}}\boldsymbol{a}_{MIMO}^H(n, \alpha)\boldsymbol{x}[n] = \frac{1}{M_{VA}}\sum_{m=0}^{M_{VA}-1}\exp\left(-j2\pi f[n]\frac{d_R}{c}m\sin\alpha\right)x[m, n], \quad (5)$$

where d_R is the distance between adjacent radar receive elements. A Discrete Fourier Transform (DFT) applied to Equation (5), thus creating a 2-D power distribution in range and angle, a range-angle map. The radar system used in the experiments has four transmitters and eight receivers. Signals are transmitted from each element in set sequence as a function of time. This allows the transmitted signals to be separately received using time de-multiplexing and hence straightforward computation of the range-angle maps:

$$J(r, \alpha) \approx \left|\frac{1}{NM_{VA}}\sum_{n=0}^{N-1}\exp\left[-j2\pi\left(\frac{2r\beta}{cN}\right)n\right]\sum_{m=0}^{M_{VA}-1}x[m, n]\exp\left[-j2\pi\left(f_0\frac{d_R}{c}\sin\alpha\right)m\right]\right|^2, \quad (6)$$

where r is the target range, α is the target angle, N is the number of recorded samples, M_{VA} is the total number of the virtual array elements, β is the effective sweep bandwidth, c is the speed of light, f_0 is the start frequency and d_R is the distance between two adjacent virtual array antennas.

2.3 | World memory map construction

The range-angle maps are the basis for creating the final perception of the area around the robot. Information is obtained from multiple range-angle maps, over multiple frames, and cumulatively combined as the robot moves. In this way the WMM is eventually created. This can be considered a form of instantaneous memory, created from the near-recent past, and helps improve detection and hence subsequent path planning.

The method used to create the WMM is part inspired by the notion of certainty grids [16]. In a *certainty grid*, the whole radar field of view is represented by a two-dimensional array of cells arranged in a Cartesian co-ordinate frame. The distance between adjacent cells is set to be the range resolution of the radar in this study, ΔR_{WMM}. Each cell in the certainty grid contains an obstacle certainty value (OCV) that represents the confidence in declaring the presence of obstacles within it. An accumulation of OCVs, over a number of radar frames, forms the obstacle certainty cumulative value (OCCV). This is the

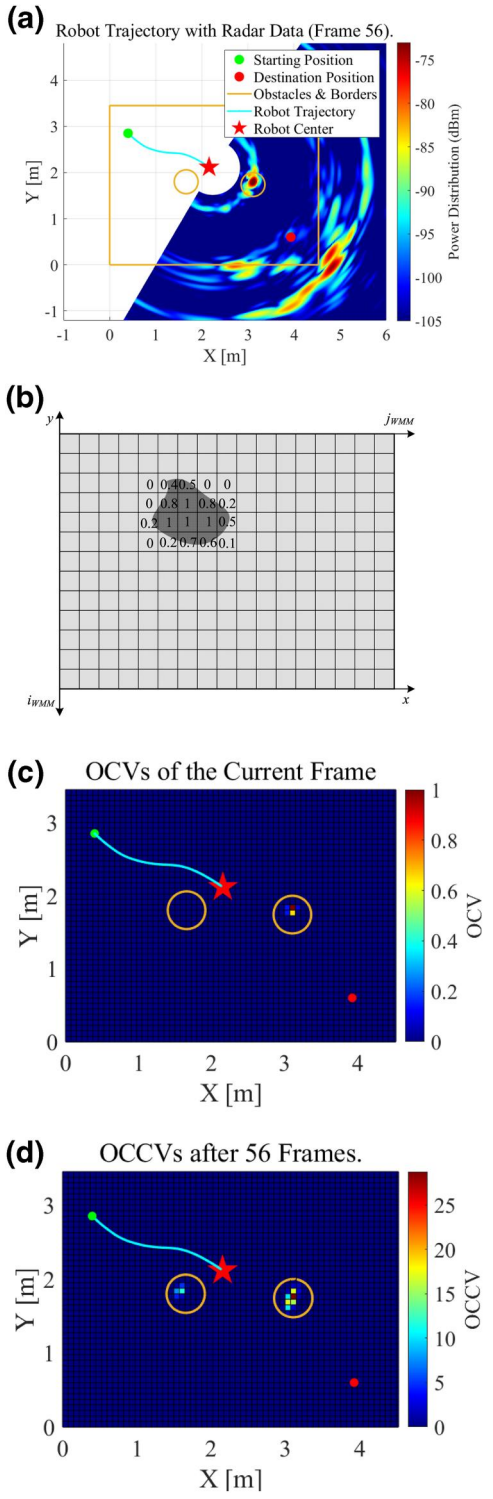

FIGURE 3 WMM construction example(a) range-angle map obtained by a single detection in rectangular coordinates, (b) OCV calculation schematic diagram. The number in each cell represents the fraction occupied by a detected obstacle, (c) OCVs of the current frame, (d) WMM after 56 frames of radar data with OCCV; OCV, obstacle certainty value; OCCV, obstacle certainty cumulative value; WMM, world memory map

value within a single cell in the WMM and the value is updated at every radar detection. To provide illustrative examples of how the radar iteratively perceives and remembers its environment through this approach, example outputs, using our experimental radar setup, are shown in Figure 3.

1) Calculate the OCV

Consider the radar range-angle map shown in Figure 3a, formed from a single radar frame (i.e. for time multiplexed transmissions processed according to Equation [6]). The radar is moving within an experiment zone, marked as the black solid line in the figure. The starting point is shown as the green dot and the final destination goal is the red dot. The range-angle map shows high echo strengths in the direct line-of-sight to the radar and, as might be expected, these are highest at close proximity, for example, at (X, Y) = (3.1, 1.7) m. These echoes correspond to an obstacle. However, echoes from beyond the experimental zone including those from the walls of the lab can also be observed.

The calculation of the OCV is a binary decision (i.e. obstacle present or not), where the amplitude in each cell of the range-angle map is compared to a radar detection threshold in a conventional manner O_{bs1}, i.e.

$$Amp_{r,\alpha} = \begin{cases} 0, & J(r,\alpha) < O_{bs1} \\ 1, & J(r,\alpha) \geq O_{bs1} \end{cases}, \tag{7}$$

where $J(r,\alpha)$ is given by Equation (6). The threshold O_{bs1} can be set at a constant value or dynamically adjusted, as for a constant false alarm rate (CFAR) detector. Here, the former approach was selected for simplicity, and the value of the set threshold was determined empirically through trial and error.

A conversion from polar to Cartesian co-ordinates subsequently follows, $Amp_{x,y} \leftrightarrow Amp_{r,\alpha}$, where $x = r\cos\theta$, $y = r\sin\theta$. The accumulated obstacle detection value of each cell is

$$\begin{aligned} &Amp_{i_{WMM},j_{WMM},n_F} = \sum Amp_{x,y} \\ &(j_{WMM}-1)\Delta R_{WMM} \leq x < j_{WMM}\Delta R_{WMM} \\ &(I_{WMM}-i_{WMM})\Delta R_{WMM} \\ &\leq y < (I_{WMM}-i_{WMM}+1)\Delta R_{WMM} \end{aligned}, \tag{8}$$

where i_{WMM} is the row index of the WMM, j_{WMM} is the column index of the WMM, I_{WMM} is the total number of rows in the WMM and n_F is the radar data frame index.

The OCV is then calculated as:

$$OCV_{i_{WMM},j_{WMM},n_F} = \frac{Amp_{i_{WMM},j_{WMM},n_F}}{\max\limits_{\substack{i_{WMM}=1,2,3,\ldots,I_{WMM} \\ j_{WMM}=1,2,3,\ldots,J_{WMM}}} \left(Amp_{i_{WMM},j_{WMM},n_F}\right)}, \tag{9}$$

where J_{WMM} is the total number of columns in the WMM.

A schematic showing the results of an OCV calculation is shown in Figure 3b. According to Equation (9), the OCV takes values between 0 and 1. It should be noticed that this value is a proportion of a single cell that is occupied by an obstacle, not an indication of likelihood regarding the presence or absence of an object. For example, a value of 0.5 in Figure 3b means that half of the cell is occupied by a detected obstacle, while the remaining half is vacant, while an OCV value of 1 means that the cell is fully occupied.

Figure 3c shows the OCVs of the range-angle map corresponding to Figure 3a. It shows that the output of the processing is a single obstacle in the vicinity of the radar, and corresponds to the actual object location in the experimental set-up. The different values in the vicinity of the obstacle show that the obstacle extends over multiple range-angle cells, and that the occupancy of the obstacle across the multiple cells is now quantified by the OCV.

2) Calculate OCCV

As the robot steers to avoid an obstacle while travelling towards its goal direction, the obstacle will eventually lie beyond the radar field of view (e.g., Figure 4).

Unless the radar 'remembers' obstacle detections and their locations from the recent past, the robot may collide with the obstacle as it attempts to steer back towards its destination goal. This becomes more problematic as the physical space that the robot has to manaeuver within decreases. The motivation behind the design of the OCCV is to address this problem whilst at the same time maximizing confidence in estimating the presence (or absence) of an object. To achieve this, the information in each cell is summed cumulatively to reduce uncertainties in cell occupancy due to the inherent variability of radar backscatter. This accumulation of detections is the main difference between the WMM and previously reported methods for generating an obstacle certainty grid [16]. Thus, a strong scatterer (e.g. a wall directly facing the radar) may appear in a particular range-angle cell. An example can be seen in Figure 3a, at (X, Y) = (2.5, 1.2) m. This is actually a response entering through the beams sidelobe. This is despite using a Hamming weighting to reduce sidelobes. Sidelobes from such strong scatterers may instantaneously exceed the radar detection threshold, O_{bs1}, and hence incorrectly be classed as obstacles. This then means the steer direction searching will incorrectly take them into account as if they are real obstacles at that location. Other instantaneous artefacts can arise due to multipath. Equally detections can be missed due to low reflectivity caused by an unfortunate combination of relative orientations of radar and object. However, in observing the scene over an extended period, from changing orientations as the robotic platform moves, it can be expected that these artefacts may either reduce or move to different range-angle cells, and hence are suppressed by the OCCV processing.

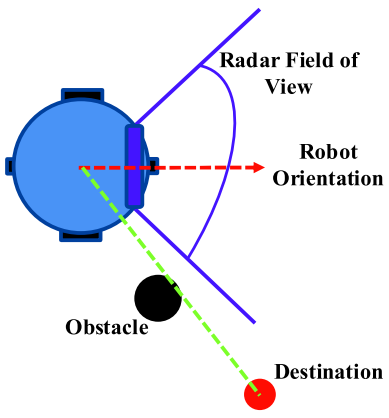

FIGURE 4 Obstacle out of radar line of sight scenario

The OCCV is based on all radar frames according to:

$$OCCV_{i_{WMM},j_{WMM},N_F} = \sum_{n_F=1}^{N_F} OCV_{i_{WMM},j_{WMM},n_F}, \quad (10)$$

where N_F is the total number of frames/range-angle maps obtained and also represents the current radar frame index. Thus, the OCCV signifies the cumulative occupancy of a range-angle cell in the current radar frame, after an accumulation of N_F radar frames. For example, assuming $N_F = 12$, an OCCV value of 12 means that the cell was 100% occupied by the target (OCV = 1) in all 12 radar frames. In Figure 3d, $N_F = 56$ but the maximum OCCV is slightly over 25, which means that the cell was not fully occupied during all radar frames. A second threshold, O_{bs2}, is then set to determine whether a detected high echo strength can be accredited to an obstacle or has resulted from a measurement artefact, in which case it is suppressed.

3 | REAL-TIME OBSTACLE AVOIDANCE

3.1 | Use of an active window

Calculating the WMM obtained over the entire field of view is computationally intensive for real-time obstacle avoidance.

To overcome this an active window (AW) is employed (Figure 5a) to limit the quantity of data to be processed [14]. If the centre of the AW is the robot centre position (i_{robot}, j_{robot}), and the AW contains $(2w_s + 1) \times (2w_s + 1)$ active cells, the OCCV of each active cell is $OCCV_{i_{AW},j_{AW},N_F}$ where

$$\begin{aligned} i_{AW} = {} & i_{robot} - w_s, i_{robot} - w_s + 1, \ldots, i_{robot}, \ldots, i_{robot} \\ & + w_s - 1, i_{robot} + w_s, \\ j_{AW} = {} & j_{robot} - w_s, j_{robot} - w_s + 1, \ldots, j_{robot}, \ldots, j_{robot} \\ & + w_s - 1, j_{robot} + w_s. \end{aligned} \quad (11)$$

Comparison of OCCV values in the AW with the threshold O_{bs2} provides a binary map of cell occupancy (Figure 5b) due to the presence of obstacles:

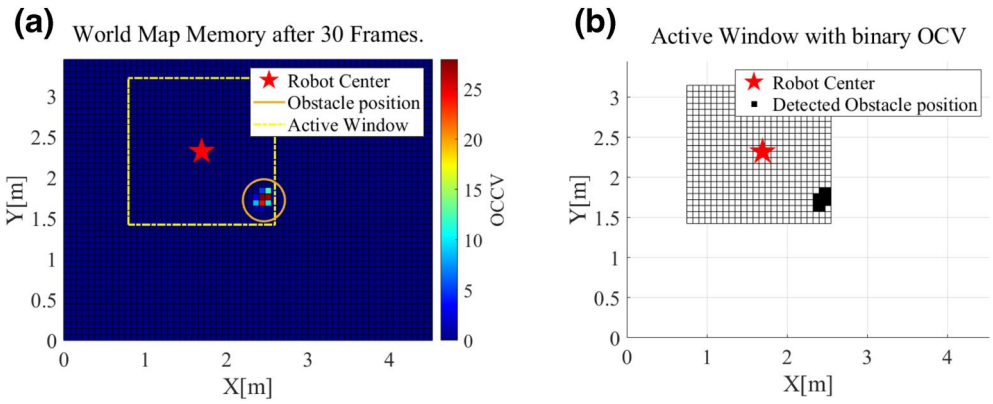

FIGURE 5 Active window (AW) selection. (a) AW position in the WMM, (b) AW with binary OCV; OCV, obstacle certainty value; WMM, world memory map

$$AW_{i_{AW},j_{AW},N_F} = \begin{cases} 0, & OCCV_{i_{AW},j_{AW},N_F} < O_{bs2} \\ 1, & OCCV_{i_{AW},j_{AW},N_F} \geq O_{bs2} \end{cases}. \quad (12)$$

Note that, the optimal number of frames, together with the optimal value of O_{bs2}, is a complex topic, requiring further research, as their values depend not only on the radar parameters, but also the navigation environment (e.g. available physical space, density of obstacles). This is beyond the scope of this study. For the purposes of the research described here the values were found by trial and were determined as $N_F = 30$ and $O_{bs2} = 2$. Given these values, a cell occupied for 7.5% or less over an accumulation of all radar frames would be registered as not containing an obstacle.

3.2 | AW cells rearrangement

The binary occupancy map is now in a form that can be used to search for an appropriate steering direction that is free of obstacles. To do this, it is computationally more efficient to convert the AW cells from a rectangular arrangement to a triangular one (Figure 6). In this configuration, the search for a steering direction becomes one-, rather than two-dimensional (i.e. steering angle instead of (x, y) co-ordinates).

The corresponding cell in the triangular arrangement map is T_{m_T,n_T}. The mapping relationship between the rectangular map and the triangular map can be written as:

$$\begin{aligned} &AW_{i_{AW},j_{AW},N_F} \leftrightarrow T_{m_T,n_T,N_F}, \\ &m_T = \max\left(i_{AW}, j_{AW}\right), \\ &n_T = \max(I_{AW}, J_{AW}) + \left(j_{AW} - i_{AW}\right), \end{aligned} \quad (13)$$

where I_{AW} is the total number of rows in the rectangular map and J_{AW} is the total number of columns.

The cells covered by a straight line between any two points in rectangular coordinates (the left hand-side of Figure 6) is the same as the cells covered by a straight line of the corresponding two points in the triangular mapping (the right hand-side of Figure 6). This means, if there are no obstacles in the cells connecting the two points in triangular mapping, the area in the rectangular coordinate system corresponding to these cells also does not include any obstacles. If the obstacle distribution in the AW is simple, one steering direction calculated according to the AW is sufficient and form the output of this step. If the obstacle distribution in the AW is complex, for example, there is no one single direction without obstacles allowing the robot to move towards to the goal position, a path planning algorithm is needed as the output of this step.

3.3 | Nearest steering vector search

A quadrilateral search window is used as shown in the triangular mapping on the right hand-side of Figure 7. The centre of the top edge of the quadrilateral corresponds to the centre of the robot. The length of the top edge depends on physical dimensions of the robotic platform. The bottom edge of the quadrilateral window is on the bottom line of the triangular map. The length of the bottom edge of the quadrilateral is determined by both the physical dimensions of the platform and, if required, a required safe distance between the platform and an obstacle that acts as an additional precaution that takes into account radar position measurement errors.

If there are no obstacles present within the quadrilateral window area, the direction from the robot centre to the centre of the bottom edge of the quadrilateral window is a feasible steering direction for the robot. A direction sequence can then be obtained as:

$$\begin{aligned} &D_{i_s} = \begin{cases} 0, & \textit{no obstacles in the } i_s \textit{ th searching window} \\ 1, & \textit{with obstacles in the } i_s \textit{ th searching window} \end{cases}, \\ &i_s = 1, 2, 3, \ldots, 2(\max(I_{AW}, J_{AW})) - d_{safe}, \end{aligned} \quad (14)$$

where d_{safe} is the safe distance from an obstacle to be maintained by the platform, expressed as a number of cells. Suppose

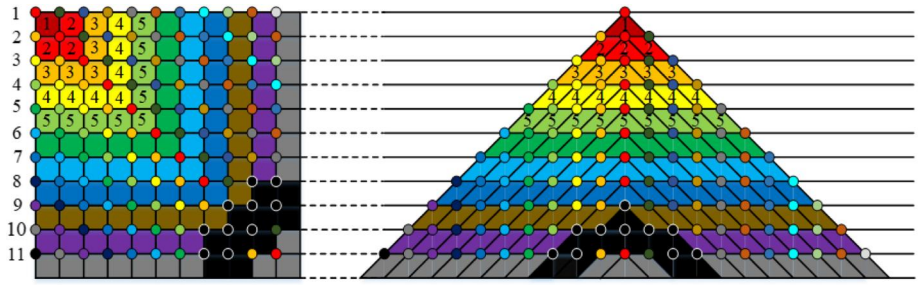

FIGURE 6 AW cell mapping relationship. The black cells represent the detected obstacles

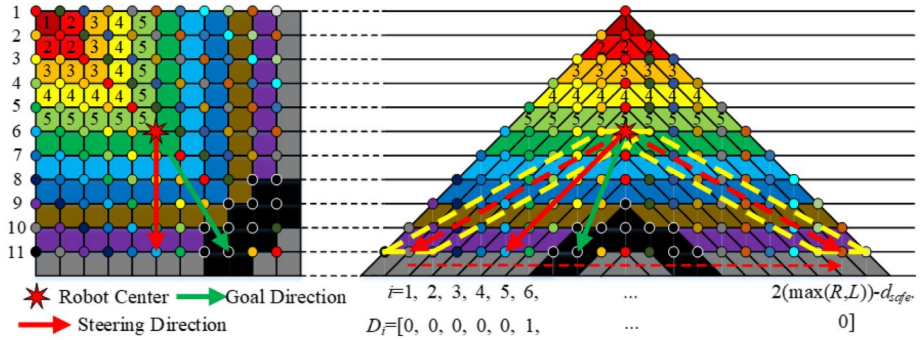

FIGURE 7 Steering direction searching. The yellow dashed box represents the searching window

the goal destination of the platform in the triangular map is$(m_T, n_T) = [\max(I_{AW}, J_{AW}), n_{goal2}]$. The steering end point (m_{dir2}, n_{dir2}) in the triangular map can be calculated as:

$$\begin{aligned} &m_{dir2} = \max(I_{AW}, J_{AW}) \\ &n_{dir2} = i_s + 1 \\ &\text{where } i_s \in \{1, 2, 3, \ldots, 2[\max(I_{AW}, J_{AW})] - d_{safe}\}, D_{i_s} = 0, \\ &|i_s - n_{goal2}| = \min_{i_s=1,2,3,\ldots,2(\max(I_{AW}J_{AW}))-d_{safe}} (|i_s - n_{goal2}|). \end{aligned} \tag{15}$$

Suppose the centre of the robot in the AW is (m_{robot1}, n_{robot1}), thus the Nearest Steering Vector to the goal direction in the AW is

$$\boldsymbol{s}_{dir1} = (n_{dir1} - n_{robot1}, m_{dir1} - m_{robot1}), \tag{16}$$

where

$$\begin{aligned} m_{dir1} &= \begin{cases} m_{dir2}, & m_{dir2} - n_{dir2} \geq 0 \\ 2m_{dir2} - n_{dir2}, & m_{dir2} - n_{dir2} < 0 \end{cases}. \\ n_{dir1} &= \begin{cases} n_{dir2}, & m_{dir2} - n_{dir2} \geq 0 \\ m_{dir2}, & m_{dir2} - n_{dir2} < 0 \end{cases} \end{aligned} \tag{17}$$

The final steering direction angle for the robot is:

$$\theta_{dir} = \text{atan } 2(m_{dir1} - m_{robot1}, n_{dir1} - n_{robot1}). \tag{18}$$

4 | EXPERIMENTAL TESTING

4.1 | Mobile robot

To assess the feasibility of the robot moving autonomously from a starting point to a final destination using the radar and processing algorithms a series of experiment were performed. The experimental platform (Figure 8 bottom left) consisted of a commercial MIMO radar system guiding the robot through a confined space with two obstacles (Figure 8). Both obstacles were of cylindrical shape. The working space for the robot is a 4.5 m × 3.5 m square free space.

The mobile platform used for experiments is a differential drive wheeled robot with a physical radius of 0.22 m (Figure 8 bottom left). The robot has two driving wheels at the sides of the body and two small caster wheels at the front and the rear of the robot. The robot is equipped with two encoders to maintain dead reckoning. Based on the signals from the encoders, the laptop can obtain the relative position and direction of the robot in a local co-ordinate frame. This was used to record the platform's route to its destination. The starting position of the robot was (0.40, 2.85) m in a custom local co-ordinate system (the origin being the bottom left corner in the enclosure shown in Figure 8), while the destination position is at (3.93, 0.60) m, i.e. near the bottom right corner of the enclosure.

The radar is Inras' Radarbook, which is a 77 GHz, FMCW, linear array MIMO radar with four transmit and eight receive elements. The receive and transmit antenna element spacings were 1.9 mm and 8 × 1.9 mm, respectively. The radar waveform characteristics used are shown in Table 1.

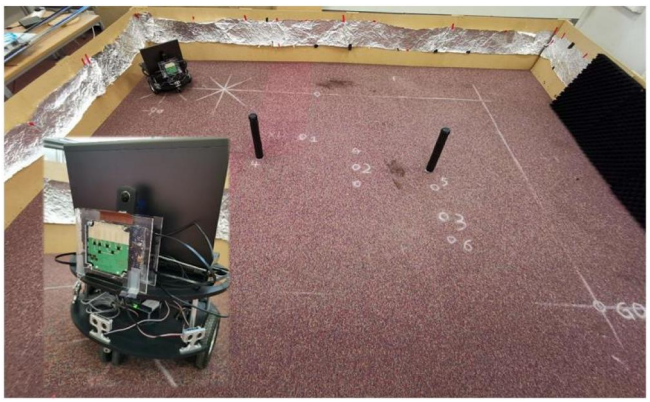

FIGURE 8 Photo of the robot and its working space with two cylindrical obstacles

TABLE 1 Radar parameters

Description	Value	Unit
Start frequency	76	GHz
Stop frequency	78	GHz
Ramp up duration	60	μs
Ramp down duration	2	μs
Sampling rate	10	MHz
Range resolution	0.132	M
Beamwidth (angular resolution)	3.151	Degrees

Both the radar and the robot were interfaced to the same laptop computer, which performed the radar signal processing and control of the robot in real-time. Lastly, the instantaneous robot location was recorded at every radar frame.

4.2 | Algorithm validation

The robot was started at an initial pose of (0.4 m, 2.85 m, $\pi/4$ rad). The latter parameter is the orientation angle of the robot (and radar), measured in a clockwise direction with respect to the x-axis. The speed of the robot was set at a constant value of 0.10 m/s, and its angular rotation speed at $\frac{\pi}{3}$ rad/s. The two cylindrical obstacles were located at (1.66, 1.80) m and (3.11, 1.74) m. The radius of each cylinder is 33 mm. The main purpose of this study is to verify the feasibility of the algorithm under relatively ideal conditions. Plastic cylindrical obstacles with same radar cross section (RCS) in all directions are chosen for the experiments. The type of obstacle will affect the robustness of the algorithm. Algorithms with dynamic threshold are added to our future work plan. In the rest of this study, for simplicity, the robot is considered as a point and the radius of the obstacles are inflated by 0.258 m to help account for radar measurement limitations.

As the robot moves, range-angle maps are generated for each radar frame according to the signal processing described in Section 2. Figure 9a and Figure 10a show two examples of such maps at different radar frames, and hence different robot positions. The starting position and the current position of the robot are also shown for reference. The maps show that as the robot moves, the radar's perception of the scene changes even though the scene itself has remained the same. Naturally, this is because the relative geometry between the radar and the scene has changed. In Frame 12 (Figure 9a), both obstacles return high intensity echoes, but so do parts of the wall around the robot, which results in high levels of sidelobes. In Frame 26 (Figure 10a), the robot has moved forwards towards the destination. In this new position, However, it can be observed that the echo intensity of the first obstacle has substantially reduced, while the robot has not yet surpassed it. This is because at the current radar position the obstacle is now outside the field of view of the radar, hence posing a collision risk. It can also be observed that reflections from the wall are approximately 15dB less than in Frame 12, highlighting the variability of radar scattering.

Figures 9b and 10b show the resulting OCVs with a detection threshold, O_{bs1}, empirically set at -77 dBm. Both obstacles are detected in Frame 12, whereas only one has been detected in Frame 26. In both cases, the percentage of full cell occupancy measured by the OCV is shown in the Figures, as well as the degree to which the obstacles extend across multiple range-angle cells.

Figure 11a is the WMM (10), accumulated from 26 frames of radar data. The figure shows both obstacles are now clearly detected, while their distribution is indicative of the variability of the scattering from the cylindrical obstacle. For 26 frames, the absolute maximum OCCV value would be 26, whereas the value measured is slightly over 12. This means that during the motion of the robot a cell was fully occupied for just under half the radar frames. As mentioned earlier, to make a binary decision on cell occupancy, a second detection threshold was empirically set at $O_{bs2} = 2$, which means that there were at least two complete obstacle detections at the corresponding cell in the WMM. The result of this process for the cells within the AW is shown in Figure 11b. The green line is the goal direction and the red line is the steering direction arising from the search result. The Figure shows that the WMM has now been converted into a binary cell occupancy map, where the location of echoes from the first obstacle are correctly marked.

4.3 | Different obstacle avoidance strategy tests

1) Different safe distances

The proposed approach also allows the setting of a safe distance, d_{safe} (14) to be maintained between the robotic platform and any nearby obstacles. To test this approach, 10 experiments were conducted with the same starting robot pose

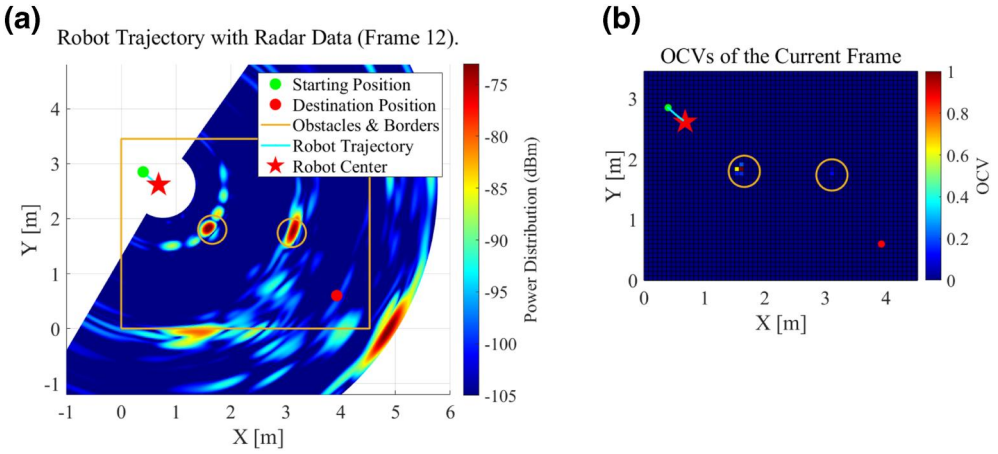

FIGURE 9 Range-angle map and corresponding OCV (Frame 12). (a) Robot trajectory with radar frame 12, (b) the corresponding OCVs of the current frame; OCV, obstacle certainty value

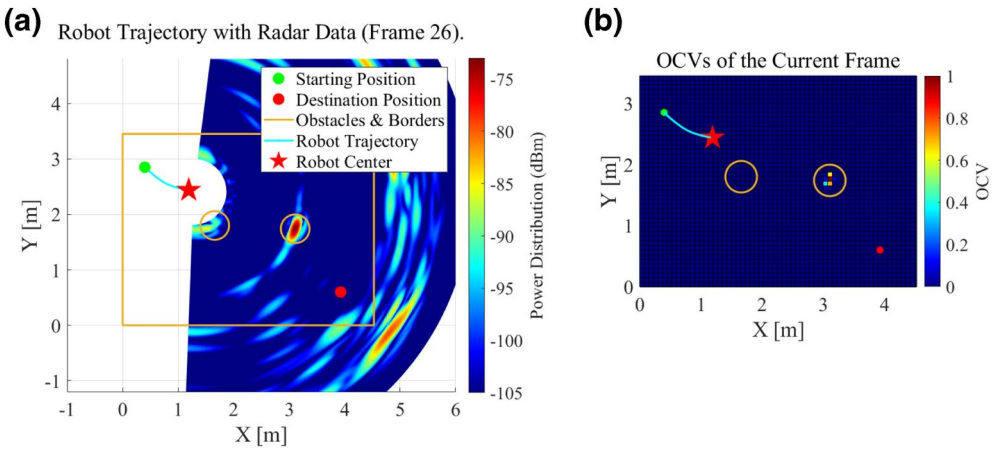

FIGURE 10 Range-angle map and corresponding OCV (Frame 26). (a) Robot trajectory with radar frame 26, (b) the corresponding OCVs of the current frame; OCV, obstacle certainty value

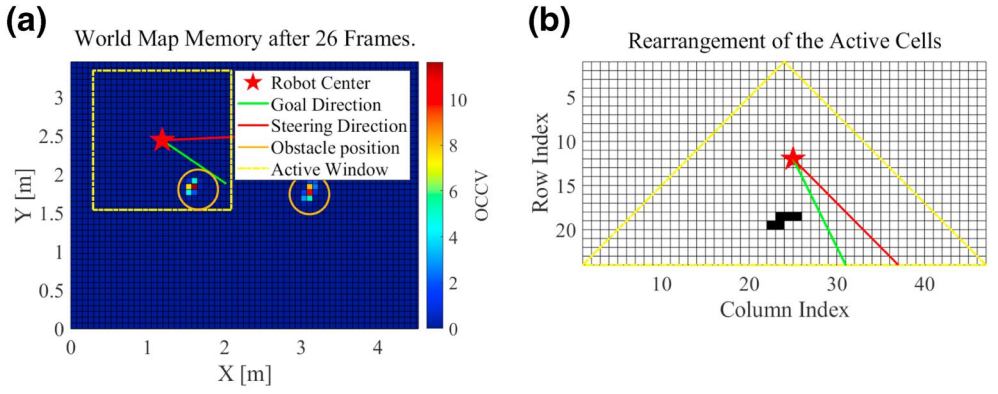

FIGURE 11 WMM accumulated from 26 frames of radar data. (a) WMM after 26 Frames, (b) cell occupancy within the AW; AW, active window; OCCV, obstacle certainty cumulative value; WMM, world memory map

and experimental setup as in the previous section, but setting d_{safe} at different values of 3, 5, 7, 9, and 11 cells, respectively. The results are shown in Figure 12, where it can be observed that the platform adjusts its trajectory to maintain the safe distance that has been set and the robot reaches its final destination without collision in all cases. It can also be

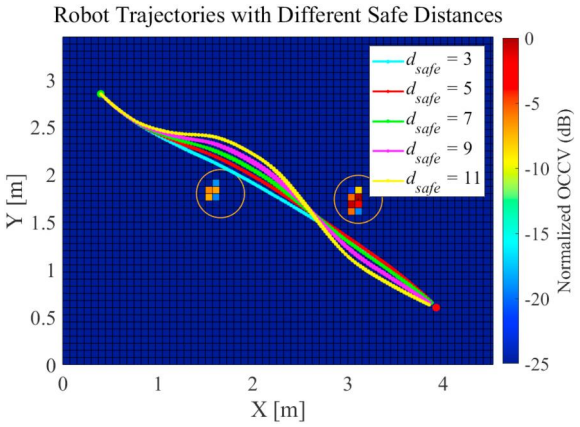

FIGURE 12 Varying the safe distance. d_{safe} is set to be the number of cells away from the detected obstacles; OCCV, obstacle certainty cumulative value

observed that the trajectory of the robot is a little different in each case. This is because very minor differences in the starting condition can result in a change in perception that, in turn, leads to a different path being taken. This is examined further next.

2) Different starting orientations.

A second set of tests were made to assess the robustness of the algorithms to different starting orientations. During these tests, the same experimental setup was used, with the same platform starting position of (0.40,2.85) m, but with initial orientations.

Figure 13 shows the results of different initial starting orientations. The initial orientations are $3\pi/2$, $7\pi/4$ and 0. The results show that as the starting pose changes, so the route of the robot towards its destination, varies even more than observed in the previous experiments. This comes as no surprise as the perception gained through the radar data will be very different across the range of starting orientations. However, in all the experiments the robot still reaches its destination without any collisions.

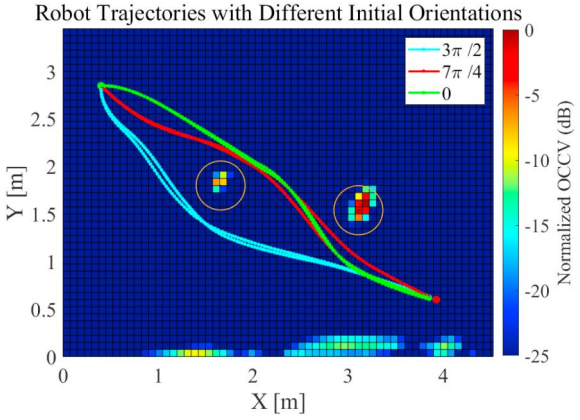

FIGURE 13 Robot trajectories with different starting orientations; OCCV, obstacle certainty cumulative value

5 | CONCLUSION

A cognitive radar architecture augmented by WMMs has been implemented and tested to show that it can be used as a basis for collision-free robotic platform navigation in confined spaces. The creation of the WMM, which mimics a radar short-term memory, is a major advantage when obstacles slip outside the field of view of the radar. Further, it enables a means of suppressing artefacts arising from variability in radar scattering which would otherwise create a false perception and degrade navigation performance. In this way the improved radar perception can form a much more reliable and robust basis for path planning and obstacle avoidance.

The radar signal processing algorithms were analytically derived and experimentally examined in real-time using an experimental platform carrying a radar sensor. The results show the feasibility of the approach, its ability to maintain user-defined safe distances from obstacles in its path, and its robustness to the relative geometry between the radar and the physical space it navigates in. However, no attempt has been made to optimize the approach and there is much further work required in order to fully validate and verify performance.

Indeed, there are several areas that can be identified for future work. Other primary areas of interest are the use of dynamic, rather than fixed, empirically set radar thresholds, dynamic adaptation of platform speed (which was kept constant in this study), and creation and exploitation radar long-term, rather than short-term memory, including the use of stored priors or map data bases. Collectively, all of these may further enhance radar decision considerably beyond that demonstrated here and hence aid navigation in more complex environments, particularly the outside world.

ACKNOWLEDGMENTS

This work was supported in part by the National Key R&D Program of China (Grant No. 2018YFE0202101, 2018YFE0202102) and the China Scholarship Counciland University of Birmingham.

CONFLICT OF INTEREST STATEMENT

Liyong Guo, Michail Antoniou and Christopher J. Baker have no conflict of interest to disclose.

ORCID

Liyong Guo https://orcid.org/0000-0002-1805-6307

REFERENCES

1. Pandey, A., Pandey, S., Parhi, D.: Mobile robot navigation and obstacle avoidance techniques: A review. Int. J. Robot. Autom. 2(3), 00022 (2017)
2. Matveev, A., Savkin, A., Hoy, M. Survey of algorithms for safe navigation of mobile robots in complex environments. Safe Robot Navigation Among Moving and Steady Obstacles, pp. 21–49. Butterworth-Heinemann, Oxford, UK (2016)
3. Viquerat, A., Blackhall, L., Reid, A., et al.: Reactive collision avoidance for unmanned aerial vehicles using Doppler radar. In: Zelinsky, A., (eds.) Field and Service Robotics, pp. 245–254. Springer, Heidelberg (2008)

4. Rouveure, R., Jean, L., Debain, C., et al.: Robot localization and navigation with a ground-based microwave radar. In: 2019 International Radar Conference (RADAR) IEEE (2019)
5. Tierney, B.B., Rodenbeck, C.T.: 3D-Sensing MIMO Radar for UAV formation flight and obstacle avoidance. In: 2019 IEEE Radio and Wireless Symposium (RWS). Orlando, FL, USA, p. 13 (2019)
6. Sarabandi, K., Vahidpour, M., Moallem, M., et al.: Compact beam scanning 240GHz radar for navigation and collision avoidance. In: George, T., Islam, M.S., Dutta, A.K. (eds.), Micro- and Nanotechnology Sensors, Systems, and Applications III. 8031, pp. 318–325. International Society for Optics and Photonics SPIE (2011)
7. Haykin, S.: Cognitive radar: a way of the future. IEEE Signal Process Mag. 23(1), 30–40 Jan (2006)
8. Guerci, J.R.: (2011). Cognitive radar: the knowledge-aided fully adaptive approach. Aeronaut. J., 115(1168), 390
9. G.M. Reich, M. Antoniou, C.J. Baker.: Memory-enhanced cognitive radar for autonomous navigation. IET Radar, Sonar Navig. 14(9), 1287–1296 (2020). https://doi.org/10.1049/iet-rsn.2019.0409
10. Guo, L., Antoniou, M., Baker, C.J.: Cognitive radar system for obstacle avoidance using in-motion memory-aided mapping. In: 2020 IEEE Radar Conference Sep. Florence, Italy (2020)
11. Borenstein, J., Koren, Y.: Histogramic in-motion mapping for mobile robot obstacle avoidance. IEEE Trans. Robot. Autom. 7(4), 535–539 (Aug 1991)
12. Haykin, S., Zia, A., Arasaratnam, I., et al.: Cognitive tracking radar. In: 2010 IEEE Radar Conference, pp. 1467–1470, IEEE (2010)
13. Bell, K. L., Johnson, J. T., Smith, G. E., et al.: Cognitive radar for target tracking using a software defined radar system. In: 2015 IEEE Radar Conference (RadarCon), pp. 1394–1399, IEEE. (2015)
14. Chavali, P., Nehorai, A.: Cognitive radar for target tracking in multipath scenarios. In: 2010 International Waveform Diversity and Design Conference, pp. 000110–000114, IEEE. (2010)
15. Smith, G.E., Alsaif, S., Baker, C.J.: Echoic flow for cognitive radar guidance. In: 2014 IEEE Radar Conference, pp. 0490–0495 (May 2014)
16. Borenstein, J., Koren, Y.: The vector field histogram-fast obstacle avoidance for mobile robots. IEEE Trans. Robot. Autom. 7(3), 278–288 (June 1991)
17. Minguez, J., Montano, L.: Nearness diagram navigation (ND): a new real time collision avoidance approach. In: Proceedings. 2000 IEEE/RSJ International Conference on Intelligent Robots and Systems (IROS 2000) (Cat. No.00CH37113), 3, pp. 2094–2100. Takamatsu, Japan (2000)
18. Sezer, V., Gokasan, M.: A novel obstacle avoidance algorithm: "follow the gap method". Robot Autonom. Syst. 60(9), 1123–1134 (2012)
19. Horne, C., Ritchie, M., Griffiths, H.: Proposed ontology for cognitive radar systems. IET Radar, Sonar Navig. 12(12), 1363–1370 (2018)
20. Feger, R., Wagner, C., Schuster, S., et al.: A 77-GHz FMCW MIMO radar based on an SiGe single-chip transceiver. IEEE Trans. Microw. Theor. Tech. 57(5), 1020–1035 (May 2009)

How to cite this article: Guo L, Antoniou M, Baker CJ. Memory-augmented cognitive radar for obstacle avoidance using nearest steering vector search. *IET Radar Sonar Navig.* 2021;15:51–61. https://doi.org/10.1049/rsn2.12012